PHYSICAL REVIEW B **89**, 174422 (2014)

Influence of La and Mn vacancies on the electronic and magnetic properties of $LaMnO_3$ thin films grown by pulsed laser deposition

Ivan Marozau,[1] Proloy T. Das,[1,2] Max Döbeli,[3] James G. Storey,[4] Miguel A. Uribe-Laverde,[1] Saikat Das,[1] Chennan Wang,[1] Matthias Rössle,[1,*] and Christian Bernhard[1,†]

[1]*Department of Physics and Fribourg Center for Nanomaterials - Frimat, University of Fribourg, Chemin du Musee 3, CH-1700 Fribourg, Switzerland*

[2]*Department of Physics and Meteorology, Indian Institute of Technology, Kharagpur, PIN-721302, India*

[3]*Laboratory for Ion Beam Physics, ETH Zurich, Schafmattstrasse 20, CH-8093 Zurich, Switzerland*

[4]*Callaghan Innovation, P.O. Box 31310, Lower Hutt, New Zealand*

(Received 22 November 2013; revised manuscript received 4 March 2014; published 20 May 2014)

With pulsed laser deposition, we have grown c axis oriented thin films of the nominal composition $LaMnO_3$ (LMO) on LSAT(001) substrates. We find that, depending on the oxygen background pressure during growth, the LMO films contain sizeable amounts of La and/or Mn vacancies that strongly influence their electronic and magnetic properties. Specifically, we show that the Mn/La ratio can be systematically varied from 0.92 at 0.11 mbar to 1.09 at 0.30 mbar of oxygen. The cationic vacancies have markedly different effects that become most pronounced once the samples are fully oxygenated and thus strongly hole doped. All as-grown and thus slightly oxygen-deficient LMO films are ferromagnetic insulators with saturation moments in excess of 2.5 μ_B per Mn ion, their transport and optical properties can be understood in terms of trapped ferromagnetic polarons. Upon oxygen annealing, the most La-deficient films develop a metallic response with an even larger ferromagnetic saturation moment of 3.8 μ_B per Mn ion. In contrast, in the oxygenated Mn-deficient films, the ferromagnetic order is strongly suppressed to less than 0.5 μ_B per Mn ion, and the transport remains insulatorlike. We compare our results with the ones that were previously obtained on bulk samples and present an interpretation in terms of the much stronger disruption of the electronic and magnetic structure by the Mn vacancies as compared to the La vacancies. We also discuss the implications for the growth of LMO thin films with well-defined physical properties that are a prerequisite for the study of interface effects in multilayers.

DOI: 10.1103/PhysRevB.89.174422 PACS number(s): 75.70.−i, 73.50.−h, 78.20.−e

I. INTRODUCTION

The discovery of the so-called colossal magnetoresistance (CMR) effect in the perovskite-type manganite materials [1] has raised a strong interest in their versatile electronic and magnetic properties [2–6]. Most of these materials are derivatives of the rare earth (R) manganites with the general formula RMnO$_3$, which are doped on the A site with lower valent cations, such as Ca^{2+}, Sr^{2+}, or Ba^{2+} [3]. Depending on the R element, as well as on the nature and the amount of the dopant, the materials exhibit a great variety of structural, electrical, and magnetic properties [4]. This leads to fascinating effects such as CMR [2,3,5], fully spin-polarized transport [4,7], a magnetic field induced insulator-to-metal transition [6], and multiferroicity [8]. It also gives rise to a variety of possible applications of the manganite perovskites as functional materials for magnetic sensors [9], magnetoresistive read-write heads for hard drives [2], random access memories [10,11], spintronics [12,13], and catalysis [14–17], as well as in the field of fundamental materials research [18,19].

The most frequently used and well-explored family is lanthanum manganite doped on the A site with alkali earth cations: $La_{1-x}A_xMnO_3$ (A: Ca, Sr, Ba). The desired properties for custom applications are usually obtained by varying the concentration of these divalent doping ions [4]. However, even for the parent compound with the nominal composition $LaMnO_3$ (LMO), it is well known that a strong variation of the electronic and magnetic properties can be achieved with defects such as Mn or La vacancies [20–24] (see the Appendix). A prominent feature of LMO is its ability to accommodate a significant amount of cationic vacancies in addition to the oxygen vacancies that are common to many transition metal perovskites [25–31].

While this strong modification of the electronic and magnetic properties of the LMO parent compound is well documented for the case of bulk LMO [20–33], there exists a lack of systematic investigations on corresponding thin films. A number of publications report the fabrication of $LaMnO_{3+\delta}$ and $La_{1-y}MnO_{3\pm\delta}$ thin films by pulsed laser deposition (PLD) [34–39], molecular beam epitaxy [40], dc-magnetron sputtering [41], atomic layer deposition [42,43], spin-coating [44], and spray-pyrolysis techniques [45]. However, in most cases the cationic composition (i.e., the Mn/La ratio) has not been determined. Especially for PLD grown films, it is commonly assumed that the cationic composition matches that of the target [34–38]. While this is often the case for PLD-grown thin films, there exist some important exceptions including the case of the LMO thin films [39].

In the following paper, we show that the cationic composition of the PLD-grown LMO films and their subsequent electronic and magnetic properties can be modified in a systematic way as a function of the deposition conditions. Specifically, we present a parametric study of the influence of the oxygen partial pressure during the PLD growth, and we

---

[*] Present address: University of Potsdam, Institute of Physics and Astronomy, Karl-Liebknecht-Strasse 24-25, D-14476 Potsdam, Germany.

[†] christian.bernhard@unifr.ch

illustrate how the desired electronic and magnetic properties of the LMO films can be obtained by selecting proper growth conditions and postdeposition annealing treatment. Good agreement is obtained with the trends in bulk LMO samples, suggesting that the vacancy engineering allows one to produce thin films with controlled properties. The latter may be used, for example, to study interaction effects and novel phenomena at the interfaces between different materials in multilayers and heterostructures [46–48]. The investigation of thin films can also help to avoid certain limiting factors and drawbacks that can occur in polycrystalline samples, e.g., due to grain boundary effects and segregation of secondary phases [21–23]. Finally, strain effects due to a lattice mismatch with the substrate can be used to tailor the properties of thin film materials [35,49].

II. EXPERIMENTAL

Thin films with a nominal composition of $LaMnO_{3+\delta}$ and thicknesses of about 100 nm were grown with the conventional PLD technique [50]. The samples were deposited using a KrF excimer laser ($\lambda = 248$ nm, pulse duration of 25 ns) operating at a frequency of 2 Hz. A sintered ceramic pellet of stoichiometric LMO with a diameter of 25 mm was used as a target. During the deposition, the target was rotated and toggled with respect to the laser beam to ensure that each pulse interacted with a "fresh" surface on the target and that no cumulative heating of the target by the laser pulses occurred. The films were deposited on (001)-oriented single crystalline $(LaAlO_3)_{0.3}(Sr_2AlTaO_6)_{0.7}$ (LSAT) substrates ($5\times5\times0.5$ mm^3). The lattice constants of the moderately hole-doped LMO bulk samples with a rhombohedral structure (0.3861–0.3911 nm [20,21,24]) are very close to the in-plane lattice parameter of the LSAT substrate (0.3868 nm). This enables an epitaxial growth of nearly strain-free, hole-doped LMO films on LSAT substrates. Unlike the $SrTiO_3$ substrates, the LSAT substrates do not undergo any structural phase transitions at low temperatures that could impact the electronic and magnetic properties of the LMO films grown on top [51,52].

At first, we performed a preliminary parametric study on the influence of the deposition conditions, such as the substrate temperature, the laser fluence, and the substrate-to-target distance. The goal was to obtain thin films with a high structural quality that contain a sizeable amount of cationic vacancies. As an indication of the latter, we used the ferromagnetic moment as deduced from the saturation value of the magnetization measured at 10 K. Based on the crystalline quality obtained from x-ray diffraction (XRD) and the ferromagnetic moment of the LMO films, we identified the following set of the best growth parameters that was used for the growth of all subsequent LMO films: laser fluence of 2.0 J cm^{-2}, substrate temperature of 825 °C, and target to substrate distance of 5.0 cm.

Using these conditions we have grown a series of LMO films for which the oxygen background gas pressure was varied between 0.11 and 0.30 mbar, as detailed in Table I. After the deposition the samples were rapidly cooled while leaving the oxygen partial pressure unchanged. After the determination of their structural, electronic, and magnetic properties, some of these as-grown LMO films were subject to a postdeposition annealing treatment. The latter was performed in a flowing oxygen atmosphere at 600 °C for 24 hours to study the influence of the oxygenation. In a preliminary study we found that no noticeable uptake of oxygen occurs up to a temperature of 500 °C, whereas at 600 °C the oxygen mobility in the LMO films is already fast enough such that a further increase of the annealing time or annealing temperature does not result in any further changes of the structural and the electromagnetic properties. This result is in line with previous findings, which suggest that the oxidation of slightly reduced LMO powders starts at about 550–600 °C [20].

The growth mode was monitored *in situ* by reflection high energy electron diffraction (RHEED) [53]. When possible (i.e., in the case of a predominant layer-by-layer growth mode), the sample thickness was evaluated from the temporal oscillations of the RHEED intensity [53].

The film topography was examined by atomic force microscopy (AFM) with an NT-MDT NTEGRA Aura microscope under ambient conditions. The root-mean-squared surface roughness (R_q) was calculated from AFM scans performed over an area of 5×5 μm^2 (512×512 points, scan speed of 1.5 $\mu m\ s^{-1}$).

TABLE I. Deposition conditions and properties of the as-grown and oxygen-annealed nominal $LaMnO_3$ thin films: oxygen pressure during growth $p(O_2)$ and postgrowth annealing treatment (as-grown or annealed in oxygen); Mn/La ratio determined by RBS; root-mean-squared roughness R_q; in-plane cell parameter b; out-of-plane cell parameter c; FWHM of the (002) LMO film Bragg peak; thermoelectric power (TEP).

$p(O_2)$, mbar; Annealing	Mn/La ratio ±3%	R_q, nm ±25%	b, nm ±0.0005 nm	c, nm ±0.0003 nm	FWHM, ° ±0.03 (002) peak	TEP, $\mu V\ K^{-1}$ ±1%
0.11, as-grown	0.92	0.5	0.3898	0.3924	0.09	+117
O_2-annealed				0.3862		+26.6
0.15, as-grown	0.94	0.7	0.3895	0.3925	0.09	
O_2-annealed				0.3866		
0.20, as-grown	0.98	1.7	0.3900	0.3943	0.17	
O_2-annealed				0.3876		
0.25, as-grown	1.02	2.2	0.3901	0.3945	0.19	
O_2-annealed				0.3876		
0.30, as-grown	1.09	6.0	0.3902	0.3925	0.14	+70.0
O_2-annealed				0.3884		+8.13

The cationic composition, i.e., the Mn/La ratio, of the LMO films was obtained from Rutherford backscattering spectroscopy (RBS) [54]. This technique has a high sensitivity to the heavier elements, whereas an accurate determination of the oxygen content is difficult to achieve due to a lower sensitivity of the RBS technique to light elements. In addition, there is the problem of the overlap of the oxygen signals that arise from the oxide thin film and the oxide-based substrate. To avoid this overlap problem for the signals of the cations in the film (La and Mn), the samples for the RBS analysis were grown on MgO(001) substrates (using the same PLD conditions). These have a significantly larger lattice parameter ($a = 0.4213$ nm) and thus a sizeable lattice mismatch with LMO of about 9%. However, due to this large lattice mismatch, the 100-nm-thick LMO films deposited on MgO exhibit a rapid strain relaxation that has been confirmed by XRD measurements. As a result, the in-plane lattice constants of the LMO films on MgO in the range of 0.3906–0.3907 ± 0.0007 nm are very close to those of the LMO films on LSAT (0.3895–0.3902 ± 0.0005 nm, Table I). It is therefore very unlikely that strain effects due to the lattice mismatch with the MgO and LSAT substrates leads to sizeable differences in the concentration of the cation vacancies of these LMO films. We note that this approach is also commonly used to evaluate the chemical composition of thin films [39,54,55]. The measurements were performed using a 2 MeV ^{4}He ion beam and a silicon PIN diode detector that was positioned at an angle of 168°. The collected RBS data were background-subtracted, as described in Ref. [56]. The Mn/La ratio was obtained from the ratio of the corresponding integrals for the Mn and La signals. It has also been verified by a simulation with the RUMP software [57]. An example of the background-subtracted experimental and simulated RBS data for a LMO film grown at $p(\mathrm{O_2})$ of 0.2 mbar is shown in Fig. 1. The experimental uncertainty of the RBS analysis for the ratio of the cation concentrations is about ±1–2%. However, we present the corresponding uncertainty interval for the Mn/La ratio of ±3% (Table I and Fig. 2), which accounts for the statistical variation of the cation stoichiometry between the samples from different batches deposited under the same conditions.

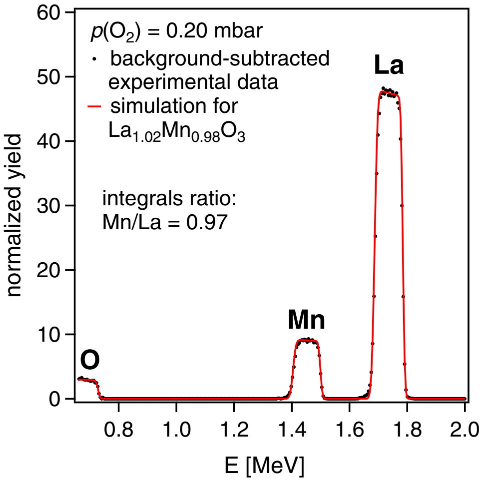

FIG. 1. (Color online) Example of the background-subtracted experimental and simulated RBS data for a LMO film grown at $p(\mathrm{O_2})$ of 0.20 mbar on a MgO(001) substrate. The substrate signal at lower energies is cut off.

The film orientation, the crystallinity, and the phase purity were investigated with XRD analysis using a four-circle Rigaku SmartLab diffractometer equipped with a rotating anode source (9 kW) yielding Cu-K_α radiation with a wavelength of $\lambda = 0.154059$ nm, parallel beam optics, and a double crystal Ge(220) monochromator. To determine the phase purity and the orientation of the films in the out-of-plane direction, we performed θ-2θ scans in the range of $2\theta = 10°$ to 80° in steps of 0.01° (1° per minute). The film thickness (d) was calculated from the Kiessig oscillations around the (001) Bragg reflection. The accuracy for the thickness determination is about ±5%. The as-grown thin films have also been examined with in-plane φ-$2\theta\chi$ XRD scans in order to check their epitaxial growth. The data was acquired in the $2\theta\chi$ range from 10° to 80° in steps of 0.008° (1° per minute) at an incident angle θ of 0.4° with respect to the sample plane. The out-of-plane and in-plane unit cell parameters of the film were calculated using Bragg's formula from the θ-2θ and φ-$2\theta\chi$ scans, respectively [58]. The experimental uncertainties are ±0.0003 nm for the out-of-plane and ±0.0005 nm for the in-plane lattice constants.

The transport properties of the LMO films were studied using a Physical Property Measurement System [(PPMS), Quantum Design] with an external Keithley 2602 System Source Meter. The resistance (R) was measured as a function of temperature (T) from 300 K down to 10 K at a cooling rate of 2 K/min using a four-probe dc technique. The data points were acquired in steps of 0.5 K. Each data point is the average of 100 fast single measurements. The measurements were performed in a constant current mode with a voltage limit of 100 mV. Depending on the sample resistance at room temperature, the driving current was varied from 100 nA to 10 μA. If the voltage limit was reached due to a very high resistance, the measurement mode was automatically changed to a constant voltage mode in which the driving current was decreased until the minimum current was reached. The upper measurement limit for the resistance is about 10^9 Ohm. The film resistivity (ρ) was calculated from the measured resistance and the film thickness, d, using the following equation for thin films, which assumes that the distance between the electrodes is much larger than d:

$$\rho = \frac{\pi}{\ln 2} \cdot R \cdot d. \tag{1}$$

The magnetization was measured using the vibrating sample option of the PPMS system, with the external magnetic field (H) applied parallel to the sample plane. The magnetization was measured as a function of temperature as the film was cooled from 300 to 10 K in a field of 1000 Oe. To determine the saturation value of the magnetization at 10 K, magnetization loops were recorded for applied fields ranging from −1 to +1 Tesla. All magnetization data were corrected for the substrate contribution, which consists of a diamagnetic signal that is T-independent and an additional weak paramagnetic signal. The latter has been found to vary between different LSAT substrates, but generally it has a noticeable effect on the signal only below ~30 K and at very high magnetic fields.

The magnetic moments have been converted to units of Bohr magnetons (μ_B) per Mn ion.

The room temperature thermoelectric power (TEP) was determined by measuring the voltage generated, while a temperature gradient of approximately 2 K cm^{-1} was maintained along the sample using a heat source of 100 mW at one end.

The optical properties of the LMO films have been investigated with a broad-band ellipsometry technique. The spectroscopic ellipsometry measurements were performed in the near-infrared to ultraviolet photon energy range of 0.5–6.5 eV with a commercial ellipsometer (Woollam VASE) equipped with an ultra-high vacuum cryostat for a temperature range of $4\text{ K} < T < 700\text{ K}$. For the far-infrared and mid-infrared ranges, we used a homebuilt setup, as described in Ref. [59], that was either attached to a Bruker 66v spectrometer at the infrared beamline of the Angströmquelle Karlsruhe (ANKA) synchrotron at Karlsruhe Institute of Technology (KIT) in Germany or to a Bruker 113v spectrometer with a glowbar light source in our laboratory. To perform the substrate correction we model the ellipsometry data using the Woollam VASE software [60].

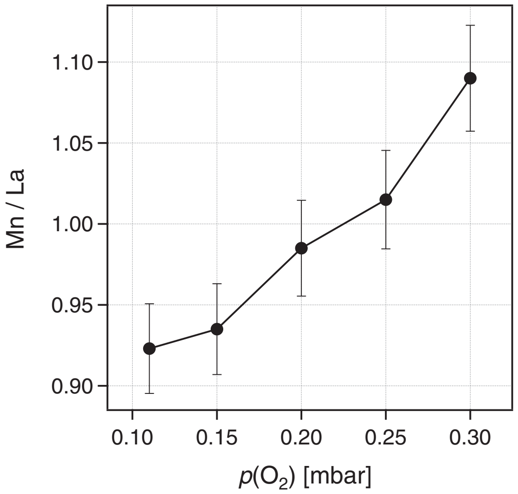

FIG. 2. Variation of the Mn/La ratio in the nominal $LaMnO_3$ films, as obtained from RBS as a function of the oxygen background pressure during deposition.

III. RESULTS AND DISCUSSION

A. Chemical composition and defects

Pulsed laser deposition is a well-established thin film deposition technique that is especially suited for the growth of materials with a complex stoichiometry [50]. Due to the high energy of the laser photons (typical $h\nu \sim 5$ eV) and the short pulse duration (~25 ns), the laser–target material interaction is predominantly photonic with only a minor degree of thermal heating [61]. Irrespective of the target's chemical composition, this results in a congruent ablation (transfer of the target material into the plasma plume). This important advantage of the PLD technique enables one to achieve a stoichiometric deposition of thin films even for chemically complex materials [50]. Nevertheless, in some cases, the stoichiometry of the film may still deviate from that of the target. One possible reason involves the complex dynamics of the ions in the plasma plume during the transfer from the target to the substrate. The most typical example concerns the loss of oxygen, which occurs since the light oxygen species are more strongly scattered on their way to the substrate than the much heavier cations [62]. This oxygen loss is usually compensated by performing the PLD growth in a background pressure of oxygen gas [50,62], which yields an extra uptake of oxygen. An additional postgrowth annealing treatment is often required to obtain the desired oxygen content in the film. Other reasons for off-stoichiometric samples can be the formation of strongly volatile species in the plasma plume [55] or the resputtering of certain elements, preferentially of the lighter elements, from the growing film that may be caused by the arriving highly energetic plasma species [62]. These processes depend on the conditions of the PLD growth, like the laser fluence and the size of the ablation area on the target, the distance between target and substrate, and the background gas pressure.

In the present study, we have varied the oxygen gas pressure to tune the cation stoichiometry of the LMO films. All samples have been deposited by ablating from a nominally stoichiometric LMO ceramic target with a Mn/La ratio close to unity. Only the background pressure of oxygen, $p(O_2)$, has been varied between 0.11 and 0.30 mbar (see Table I). The RBS analysis confirms that the Mn/La ratio in these films exhibits a systematic variation as a function of the $p(O_2)$. As listed in Table I and shown in Fig. 2, the Mn/La ratio increases systematically with growing $p(O_2)$. At 0.11 mbar the samples are strongly Mn deficient ($Mn/La = 0.92 \pm 0.03$), while at 0.30 mbar they are substantially La deficient ($Mn/La = 1.09 \pm 0.03$). A Mn/La ratio close to unity is obtained for the samples grown at $p(O_2)$ of 0.20–0.25 mbar. A possible reason for the observed Mn deficiency of the films grown at lower $p(O_2)$ is a preferential resputtering of the lighter Mn atoms by the high energy ions from the arriving plasma plume, for which the kinetic energy increases at lower $p(O_2)$. The observed preferential La deficiency of the films deposited at 0.30 mbar remains a surprising result that cannot be explained by the resputtering scenario. It may be due to the formation of La-enriched volatile clusters in the plasma or at the surface of the growing film. Likewise, the LMO system may have an intrinsic tendency to form La vacancies rather than Mn vacancies.

We remark that with the RBS technique, one can determine rather accurately the ratio of the Mn and La concentrations, whereas the determination of the oxygen stoichiometry is not possible with a sufficient accuracy due to the lower sensitivity of RBS to the light elements (like O) as well as due to the overlap of the oxygen signal with the one of the substrate. Based on the RBS data alone, we can therefore not tell whether in LMO films with a Mn/La ratio close to unity the Mn and La vacancies are absent or whether they are present in equal amounts. The latter is more likely, as is shown below based on the electric transport and magnetization data, which indicate that the films grown at a $p(O_2)$ of 0.15–0.2 mbar are in a ferromagnetic insulating state. From the RBS data we can also not determine the amount of the oxygen vacancies in the as-grown films, although we expect that these are almost absent in the films that have been annealed in oxygen atmosphere.

The comparison of the electronic and magnetic properties of the LMO films with those of the bulk LMO samples, for which the concentration of the cationic and oxygen vacancies has been reported [20,21,24], establishes the following trends: (i) all our PLD grown samples contain substantial amounts of cationic defects; (ii) the samples grown at the lowest $p(O_2)$ contain mostly Mn vacancies; (iii) for the samples grown at the highest $p(O_2)$, the vacancies are predominantly on the La sites; (iv) the as-grown samples contain a substantial amount of oxygen vacancies that are removed upon annealing in oxygen atmosphere at 600 °C; and (v) the samples are hole doped, the hole doping level is similar among the as-grown films, and it increases upon O_2 annealing.

B. Growth and microstructure

The oxygen background pressure also has a strong influence on the growth mode and the microstructure of the films. The

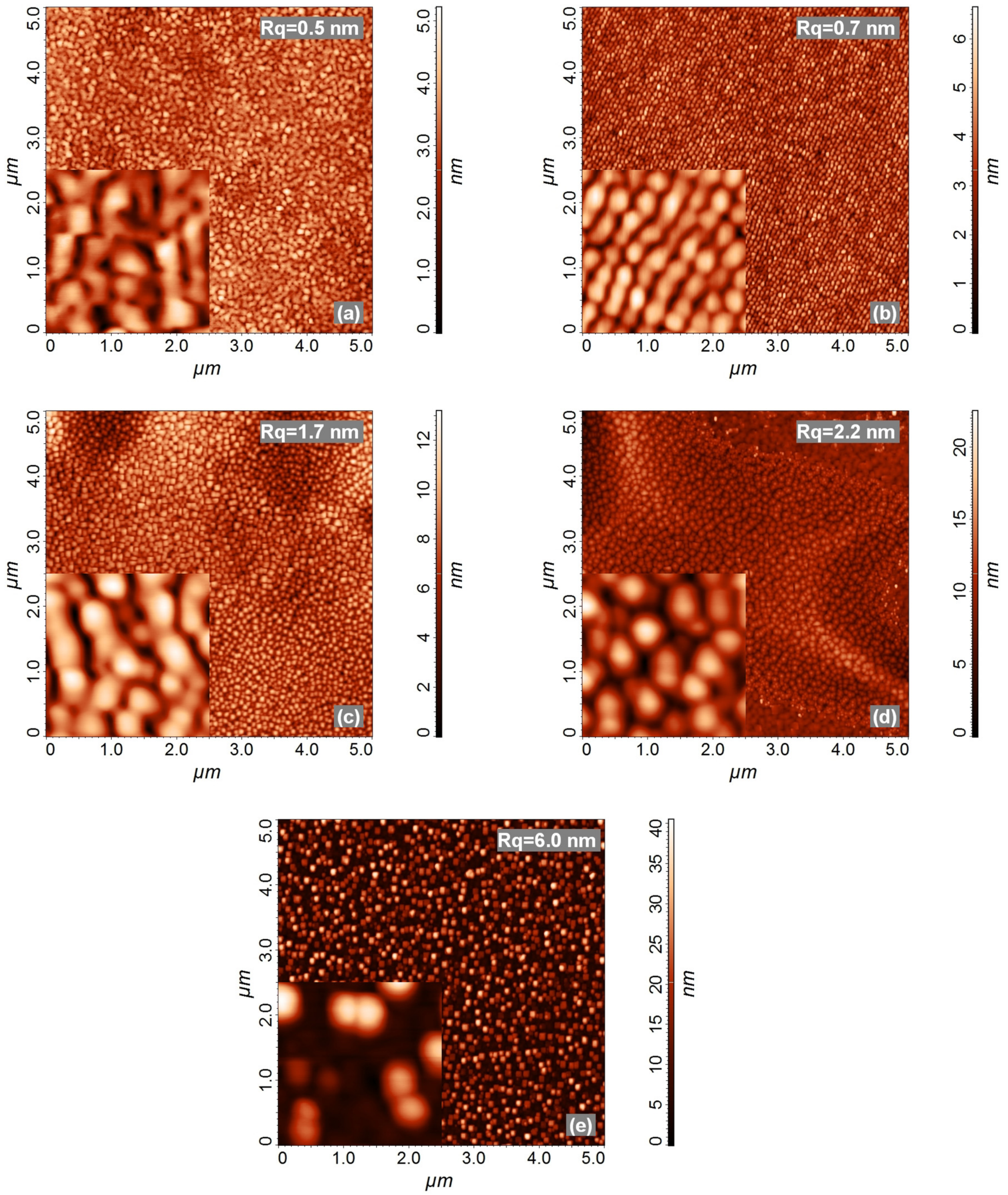

FIG. 3. (Color online) AFM images of the as-grown LMO films in (a) 0.11 mbar O_2; (b) 0.15 mbar O_2; (c) 0.20 mbar O_2; (d) 0.25 mbar O_2; and (e) 0.30 mbar O_2. The numerical insets in the top right corners give the root-mean-squared roughness; the image insets in the bottom left corners are the additional scans over an area of 500 × 500 nm^2 to show the detailed growth morphology.

growth mode was monitored *in situ* during the PLD process by RHEED, and the film microstructure was examined by AFM. The deposition of LMO at the lower $p(O_2)$ of 0.11 and 0.15 mbar results in a layer-by-layer two-dimensional growth and yields very smooth films with a low surface roughness on the subnanometer scale [see Table I and Figs. 3(a) and 3(b)]. At higher oxygen background pressures of 0.20–0.25 mbar, the growth mode changes and becomes spatially inhomogeneous with regions of two-dimensional and three-dimensional growth, yielding a complex topography of the sample surface with an increased roughness [see Figs 3(c) and 3(d)]. Finally, at 0.30 mbar the growth mode appears to

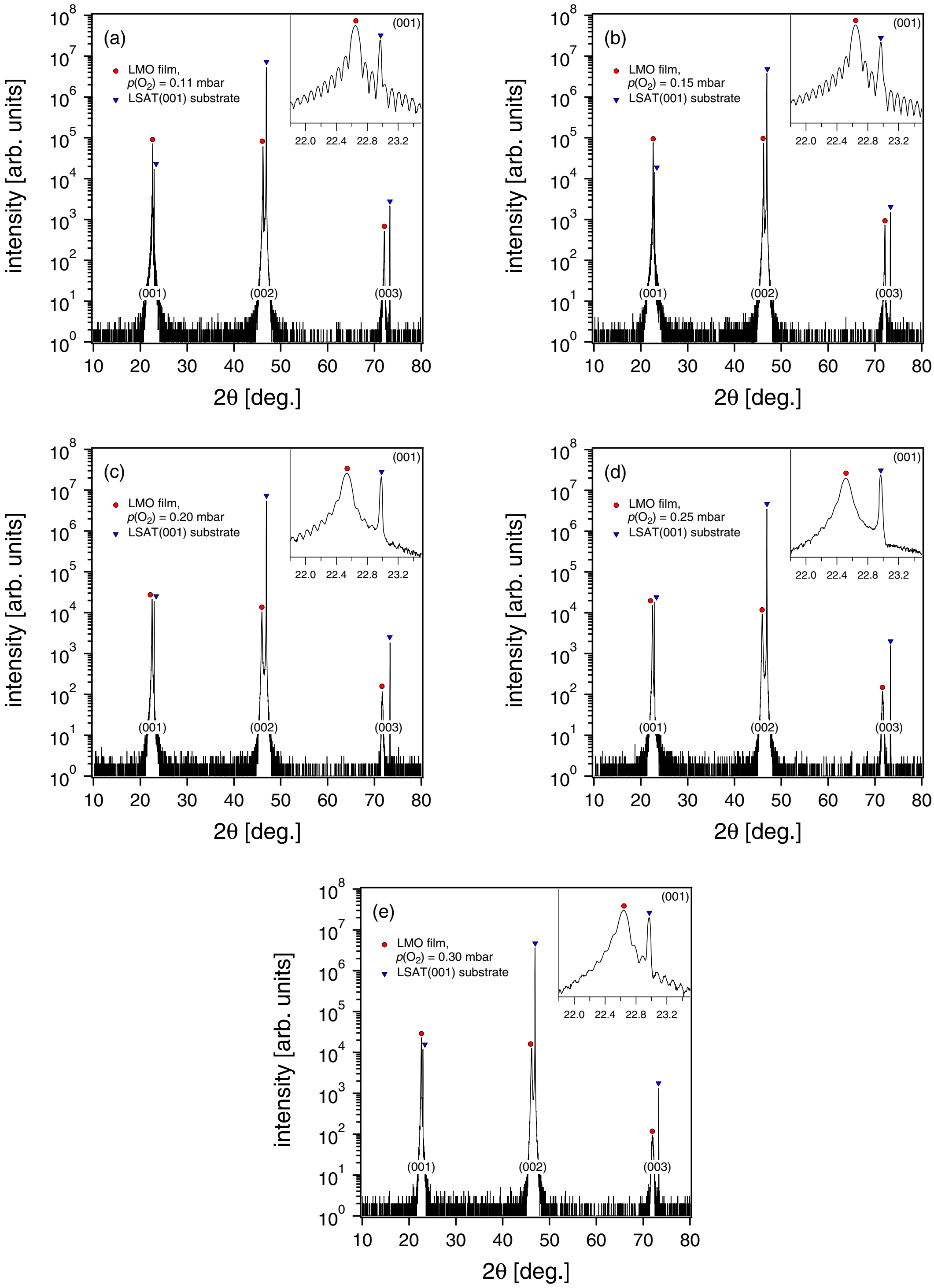

FIG. 4. (Color online) Out-of-plane XRD patterns of the as-grown LMO films. The presence of only the $(00L)$ Bragg peaks of LMO confirms the c axis oriented growth on the LSAT(001) substrates. The inserts detail the region around the (001) Bragg peak of LMO where the appearance of Kiessig fringes indicates a low roughness and homogeneous film thickness. Their periodicity has been used to determine the film thickness.

be homogeneously three-dimensional. This results in a rough surface with a pronounced granular structure [see Fig. 3(e)]. These changes of the growth mode as a function of $p(O_2)$ are indicative of a substantial variation in the mobility of the addions and the subsequent crystal lattice formation on the surface of the growing film. The two-dimensional growth at lower $p(O_2)$ suggests that the plasma species arriving at the surface have a sufficiently high energy and, thus, surface mobility to enable a layer-by-layer growth mode. As mentioned above, these high energy ions may be responsible for the Mn deficiency of the films deposited at lower $p(O_2)$. With increasing oxygen background pressure, the energy of the plasma species decreases. This reduces the surface mobility of the ions such that the growth mode changes over from a two-dimensional to a three-dimensional one.

C. Structure and lattice constants

The structural quality, the phase purity, and the out-of-plane and in-plane lattice parameters of the LMO films have been characterized with XRD measurements. The out-of-plane θ-2θ diffraction patterns, as shown in Fig. 4, reveal only the (00L) series of LMO reflections along with the corresponding reflections of the (001)-oriented LSAT substrate. This confirms that the films are fully c axis oriented. The full width at half maximum (FWHM) of the LMO (002) peaks is given in Table I. It ranges from 0.09° to 0.19° ± 0.03°, which is ∼3–6 times larger than the FWHM = 0.03° of the LSAT substrate (002) peaks. The difference is reasonably small, indicating a good film crystallinity and homogeneous out-of-plane orientation. The smoother films grown at lower $p(O_2)$ reveal narrower Bragg peaks and therefore a better out-of-plane orientation as compared to the rougher films grown at higher pressures (Table I). The presence of pronounced Kiessig fringes on the diffraction patterns of the LMO samples deposited at lower $p(O_2)$ [inserts in Figs. 4(a) and 4(b)] confirms their low roughness and uniform thickness. The absence of any extra peaks in the diffraction patterns testifies for the phase purity of these films.

The in-plane ($a = b$) and the out-of-plane (c) lattice constants of the LMO films grown in different oxygen background pressures are shown in Table I and Fig. 5(a). The in-plane cell parameters do not exhibit any pronounced dependence on $p(O_2)$ and do not change much after the postdeposition oxygen annealing. They range between 0.3895 and 0.3902 nm ± 0.0005 nm, which is quite close to the in-plane lattice constant of the LSAT substrate of 0.3868 nm. This indicates a good lattice matching between the LSAT substrate and the deposited LMO films.

The out-of-plane cell parameters of the as-grown films are larger and range from 0.3924 to 0.3945 nm ± 0.0003 nm (see Table I). Figure 5(b) shows that for all LMO films the postgrowth oxygen annealing treatment at 600 °C leads to a sizeable decrease of the c axis parameter. Since the ionic radius of Mn^{4+} is smaller than that of Mn^{3+} [63], this is a clear indication that this annealing treatment gives rise to a significant uptake of oxygen and thus an enhanced hole doping effect. We assume that all O vacancies that are present in the as-grown samples are cured by this annealing treatment. This is supported by our finding that no further changes of the c axis lattice constant or of the electronic and magnetic properties occur upon increasing the annealing duration or temperature. It is also noteworthy that the out-of-plane unit cell parameters for both as-grown and O_2-annealed films tend to increase with increasing the deposition pressure (i.e., with decreasing the amount of Mn vacancies), with the exception of the as-grown films at 0.30 mbar [see Fig. 5(b) and Table I]. This can be attributed to the disturbance of the of Mn-O-Mn network by the missing Mn species, which leads to an overall decrease of the occupied crystal lattice volume and consequently to a more compact ion arrangement with decreased average bond distances. A corresponding decrease of the lattice constant with increasing the Mn deficiency was previously also observed in bulk LMO samples [21].

D. Electrical properties

Next we discuss the changes in electrical resistivity, ρ, of the LMO films as a function of the $p(O_2)$ during growth and the

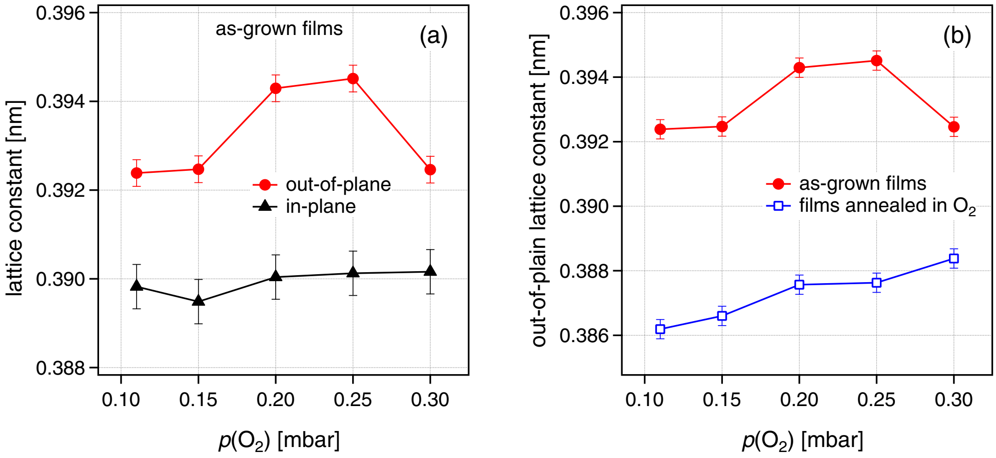

FIG. 5. (Color online) (a) Variation of the in-plane and out-of-plane lattice constants of the as-grown LMO films as a function of the oxygen background pressure during deposition. (b) Comparison of the out-of-plane lattice parameters before and after the postgrowth oxygen annealing treatment of the films.

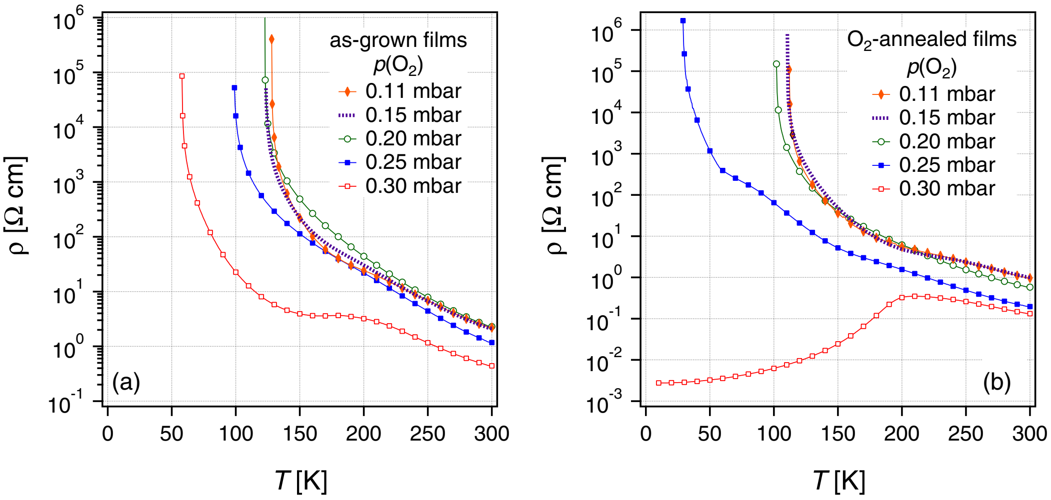

FIG. 6. (Color online) Temperature dependence of the resistivity of the LMO films: (a) as-grown samples; (b) oxygen-annealed samples. All samples except for the most La-deficient film after the oxygen annealing treatment exhibit an insulatorlike behavior. The latter becomes metallic below 200 K.

postgrowth oxygen annealing treatment. The T dependence of ρ is displayed in Fig. 6(a) for the series of as-grown LMO films and in Fig. 6(b) for the same films after the oxygen annealing treatment. All as-grown samples in Fig. 6(a) exhibit an insulatorlike behavior with a steep upturn of $\rho(T)$ below about 150 K towards very large values at low temperature that eventually exceed the upper sensitivity limit of our setup. The absolute values of $\rho(T)$ are rather similar for most of the films. The only exception is the strongly La-deficient film for which $\rho(T)$ is significantly lower, and a shoulderlike feature develops

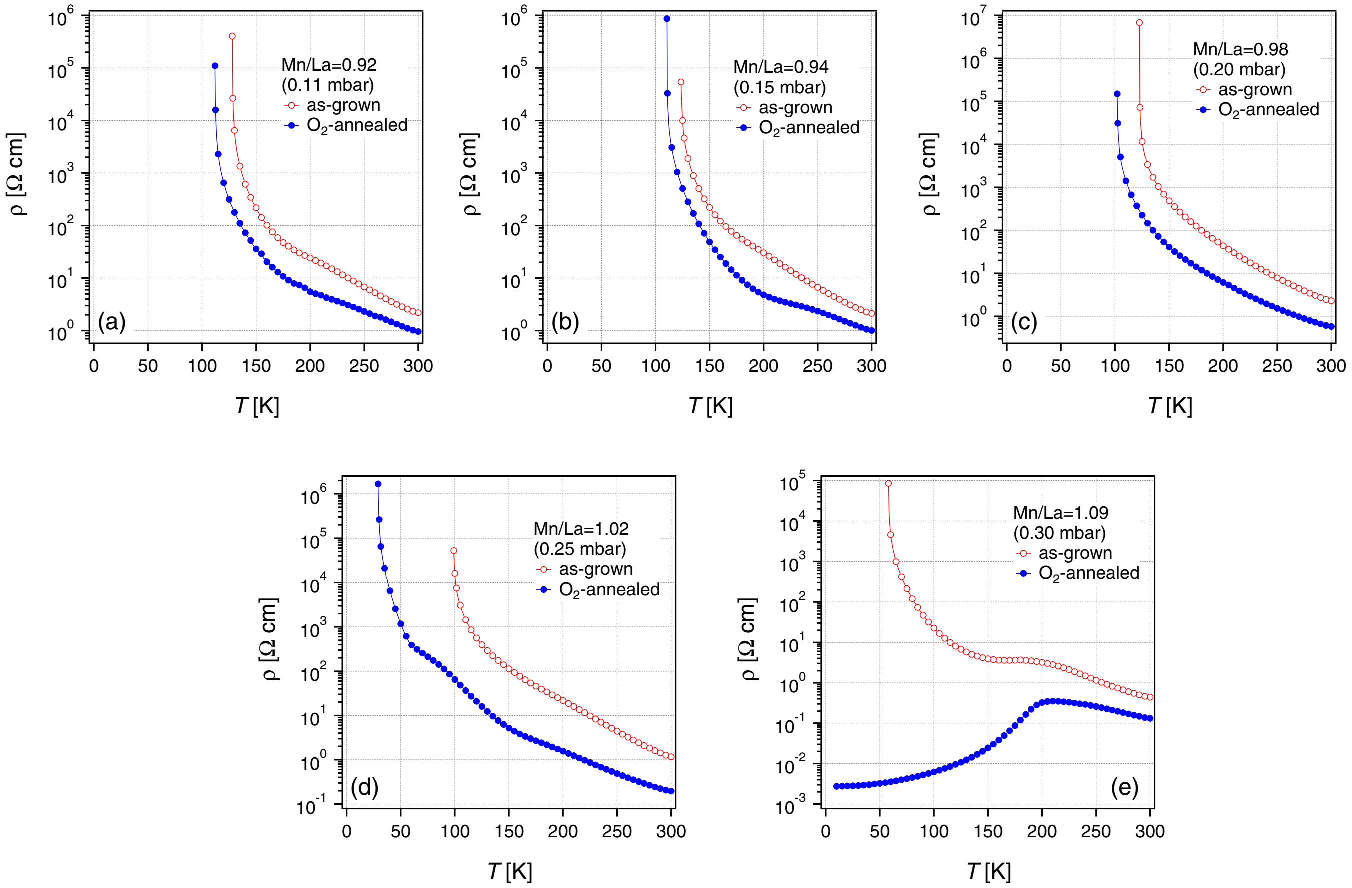

FIG. 7. (Color online) Temperature dependence of the resistivity of the LMO films before and after the postgrowth oxygen annealing treatment.

below ~200 K. The latter is related to the ferromagnetic transition, as is further discussed in the next section in the context of magnetization data. The oxygen annealing treatment leads to a significant decrease of the resistivity for all the LMO films. This is explicitly shown in Fig. 7, which directly compares the $\rho(T)$ curves for each LMO film in the as-grown and the oxygen-annealed states. For the Mn-deficient films in Figs. 7(a)–7(c), the values of $\rho(T)$ decrease by about one order of magnitude, whereas the insulatorlike shape remains almost unchanged. For the slightly La-deficient sample with a Mn/La ratio of 1.02 in Fig. 7(d), the decrease of $\rho(T)$ is already larger, but $\rho(T)$ still exhibits an insulatorlike upturn towards low T [Fig. 7(d)]. The most prominent changes occur for the strongly La-deficient film in Fig. 7(e) for which the resistivity in the oxygen-annealed state exhibits a pronounced decrease below about 200 K towards a strongly metallic state. The shape of the $\rho(T)$ curve with a cusp around the Curie temperature of about 200 K (see Sec. III E), and even the absolute low T value of $\rho(10\text{ K}) \approx 3 \times 10^{-3}\ \Omega$ cm is similar to that of $La_{0.67}Ca_{0.33}MnO_3$ or $La_{0.67}Sr_{0.33}MnO_3$ [64], for which a combined metallic and ferromagnetic state develops below T^{Curie} by the virtue of the long range double-exchange mechanism. These results demonstrate that the Mn and La vacancies, while giving rise to a similar hole doping levels, have widely different effects on the conduction mechanism in these LMO films. The doping on the La site, either by introducing La vacancies or by the substitution of La with Ca or Sr, apparently has very similar effects on the electronic properties and can be used to introduce a metallic state that is based on the so-called double exchange Mn^{3+}-O-Mn^{4+} interactions. On the contrary, the doped holes introduced by the Mn vacancies remain strongly bound to these defects, which strongly disrupt the network of Mn-O-Mn bonds. As was already mentioned in the introduction, corresponding behavior in the transport properties has been observed for bulk LMO samples in Ref. [21] where it has also been interpreted in terms of a strong trapping of holes by Mn vacancies [20,33].

The room temperature values of the TEP that was measured for some of the LMO films are summarized in Table I. Their positive values confirm that the doped charge carriers have a holelike character [65]. The absolute values are larger for the Mn-deficient films than for the La-deficient ones; for all samples they are significantly lower after the oxygen annealing treatment, which removes the oxygen vacancies. The TEP data thus confirms that the concentration and/or the mobility of the holes is higher for the La-deficient films and increases significantly upon oxygen annealing.

E. Magnetic properties

Next we discuss the magnetic properties of the LMO films. The thermal dependence of the field-cooled magnetization in an external field $H = 1000$ Oe is shown in Fig. 8(a) for the as-grown LMO films and in Fig. 8(b) for the same samples after the oxygen annealing treatment. The comparison of the magnetization loops obtained at 10 K of the as-grown and the oxygen-annealed films is shown in Fig. 9. All of the as-grown films exhibit a sizeable ferromagnetic component with a saturation moment of about 2.5–3.5 μ_B per Mn ion. This confirms that they are located in the ferromagnetic insulator regime of the phase diagram and thus are substantially hole doped due to the cationic vacancies [20,21,24]. The doping may be a bit higher for the more La-deficient samples, as is suggested by the gradual increase of the Curie temperature, T^{Curie}, from about 120 K for the most Mn-deficient sample to about 180 K for the most La-deficient film. Although, the magnetization data reveal signatures that these films exhibit a certain degree of inhomogeneity that may arise from a variation in the local concentration of the Mn and La vacancies. One example is the weak onset of the ferromagnetic signal around 200 K that occurs even for the as-grown samples at $p(O_2) \leqslant 0.20$ mbar. Another example is the weak decrease of the magnetization of the La-deficient as-grown samples at 0.30 and 0.25 mbar below about 100 K that is indicative of a small antiferromagnetic fraction due to Mn-deficient regions.

The oxygen vacancies are removed in the oxygen-annealed LMO films. The decreasing values of the c axis lattice constant, the electric resistivity, and the TEP all confirm that the oxygen annealing treatment leads to a significant increase

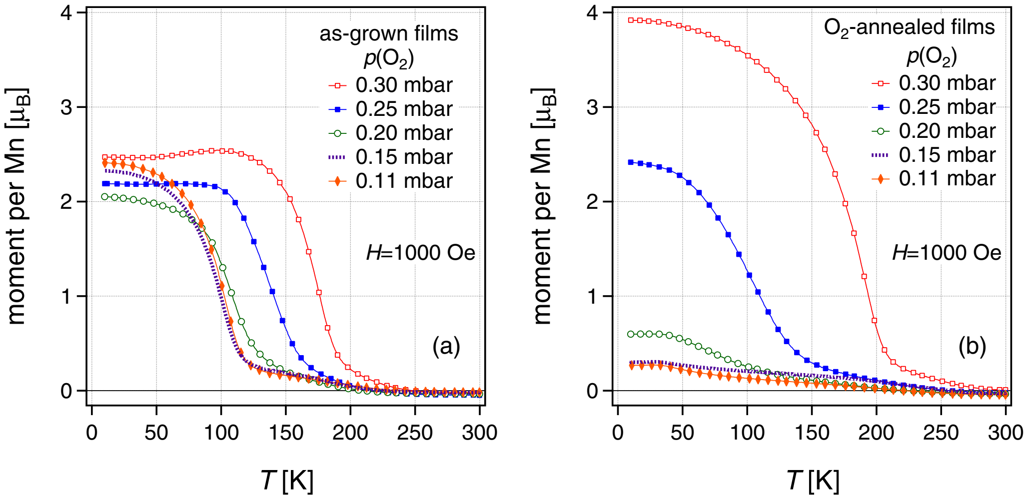

FIG. 8. (Color online) Temperature dependence of the magnetization of the LMO films measured in field-cooled mode with an external field of 1000 Oe: (a) as-grown samples; (b) oxygen-annealed samples.

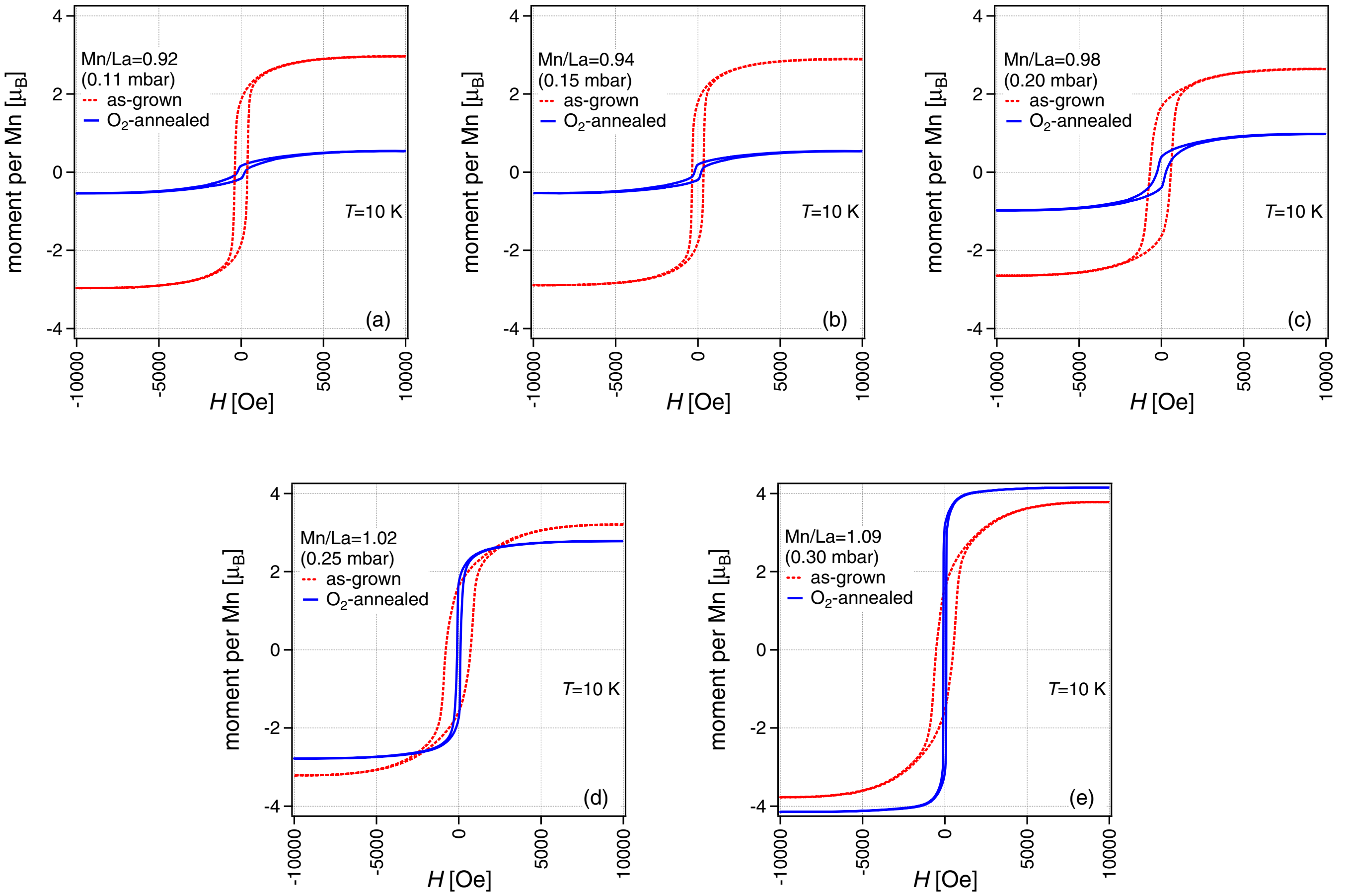

FIG. 9. (Color online) Magnetization loops of the LMO films measured at $T = 10$ K before and after the oxygen annealing treatment.

of the oxygen content (it is expected to remove the oxygen vacancies that are created during the PLD growth but not to affect the cationic vacancies). Figure 8(b) shows that for the most La-deficient films this additional hole doping yields a significant increase in the magnitude of the ferromagnetic moment to about 3.8 μ_B per Mn ion. This value is close to the theoretical limit and to the maximal value that is observed in bulk $La_{0.67}(Ca,Sr)_{0.33}MnO_3$ [64]. In combination with the strongly metallic response below T^{Curie} [as shown in Figs. 6(b) and 7(e)], this confirms that the most La-deficient samples are in the metallic ferromagnetic state, which is known to occur at a higher hole doping.

Figures 8(b) and 9(a)–9(c) show that the corresponding oxygen-annealed LMO films, which contain a large amount of Mn vacancies, have fundamentally different magnetic properties. As opposed to the further increase of the ferromagnetic moment in the strongly La-deficient sample, the ferromagnetic moment is now strongly suppressed from about 2.5 μ_B per Mn ion in the as-grown state to about 0.5 μ_B per Mn ion in the oxygenated state (Fig. 8). Notably, this drastic suppression of the ferromagnetic order occurs despite the removal of the oxygen vacancies and the concomitant increase in hole doping. The evolution of this suppression of the static magnetic order as a function of the Mn/La ratio of the LMO films is summarized in Fig. 10, which compares the saturation magnetization at 10 K for the as-grown LMO films (solid circles) with the oxygen-annealed ones (open squares). We note that a corresponding suppression of the ferromagnetic order has been observed in strongly hole doped bulk LMO samples with a large Mn deficiency [20,21,24].

The drastic suppression of the ferromagnetic order in these Mn-deficient samples upon additional hole doping due to the

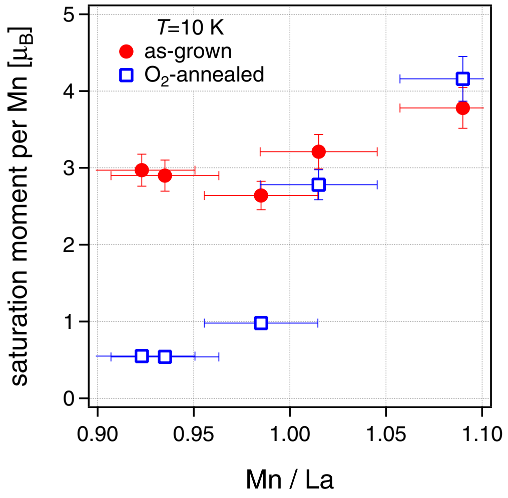

FIG. 10. (Color online) Saturation magnetization versus the Mn/La ratio of the LMO films as obtained from the 10 K magnetization loops in Fig. 9.

removal of the oxygen vacancies remains to be understood. It may well reflect the different orbital states and competing interactions that are underlying the ferromagnetic order in the insulating and metallic states. In the insulating ferromagnetic state the doped holes are forming polaronic clusters with a short-ranged ferromagnetic exchange interaction around the Mn^{4+} ions that is enabled by a special kind of local orbital order, as described in Ref. [66]. The ferromagnetic order of these polaronic clusters seems very robust and only moderately affected by the Mn vacancies. However, the destructive effect of the Mn vacancies on the ferromagnetic order appears to be strongly enhanced as the hole doping (or the Mn^{4+} concentration) is further increased. A similar trend was observed in strongly Mn-deficient bulk LMO samples for which neutron diffraction studies and magnetization measurements showed that upon further hole doping the ferromagnetic insulating state gives way to a glassy magnetic state with a high degree of frustration and disorder [24]. While it is easily understood that the Mn vacancies may inhibit the formation of a fully itinerant ferromagnetic state, it is surprising that even the localized ferromagnetic polarons are strongly suppressed by the additional hole doping (since the Mn vacancies should not be affected by the oxygen annealing at 600 °C). This suggests that the specific kind of orbital order around the Mn^{4+} ions, which is required for the formation of the ferromagnetic polarons, becomes unstable if the hole doping level (and thus the concentration of Mn^{4+} ions) exceeds a certain threshold value. This conjecture is supported by studies on bulk materials, which showed that the orbital order and especially the Jahn-Teller distortion become weaker with hole doping and disappear in the ferromagnetic metallic state [24].

We remark that even for the case of the strongly La-deficient films, there exists a clear difference in the properties of the ferromagnetic state in the insulating regime at lower hole doping and the itinerant state at larger doping. This can be seen from Fig. 9(e), which compares the magnetization loops at 10 K for the sample in the as-grown and the oxygen-annealed states. In the low-field regime, the former exhibits a significantly wider hysteresis loop and a more gradual upturn of the magnetization towards high fields. This suggests a larger crystalline anisotropy with an easy axis that is not parallel to the external field (which is applied along the film plane). This characteristic difference is also consistent with the involvement of an orbital order in the insulating ferromagnetic state and its absence in the itinerant ferromagnetic state.

F. Optical properties

Finally, we discuss the optical data, which confirm the significant differences in the electronic and magnetic properties of the La- and the Mn-deficient LMO films. Figure 11 shows an overview of the temperature dependence of the real part of the optical conductivity, σ_1, of the LMO films in the range from 0.01 to 6.5 eV. Previous optical studies on $\mathrm{La}_{0.67}(\mathrm{Ca,Sr})_{0.33}\mathrm{MnO}_3$ crystals have shown that the transition from a paramagnetic insulator or bad conductor to a ferromagnetic metal is accompanied by a sizeable redistribution of spectral weight from high energies above 2 eV to low energy where it gives rise to a free-carrierlike response [67,68]. The spectral weight of the itinerant carriers was found to roughly scale with the square of the ferromagnetic moment [67,69]. This can be understood in terms of the competition between the local Jahn-Teller distortions and the double-exchange mechanism for which the strength of the ferromagnetic coupling is determined by the gain in the kinetic energy of the delocalized spin polarized charge carriers.

Figure 11 shows that such a characteristic redistribution of the spectral weight below T^{Curie} from high to low energies also occurs in our ferromagnetic LMO films. The strongest effect is observed in the oxygen-annealed LMO film grown at 0.30 mbar in Fig. 11(b) for which a pronounced free carrier peak develops below $T^{\mathrm{Curie}} \approx 200$ K. An additional low-energy band, which appears around 0.3 eV, is likely due to polaronic effects. The spectral weight that is redistributed to below 0.8 eV into the free carrier peak and the polaronic band amounts to $\sim 4.6 \times 10^6\ \Omega^{-1}\ \mathrm{cm}^{-2}$, corresponding to a plasma frequency of $\omega_{\mathrm{pl}} \approx 13\,200\ \mathrm{cm}^{-1}$. Assuming that the effective mass of the charge carriers equals the free electron mass, their effective concentration amounts to $N_{\mathrm{eff}} \approx 1.88 \times 10^{21}\ \mathrm{cm}^{-3}$ or a concentration of 0.12 electrons per Mn ion. Similar values have been derived for $\mathrm{La}_{0.67}(\mathrm{Ca,Sr})_{0.33}\mathrm{MnO}_3$ single crystals in the itinerant ferromagnetic state [67,68,70].

Figure 11(a) shows that a somewhat modified and weaker spectral weight transfer from high to low energy occurs for the 0.30 mbar LMO sample in the as-grown state. The conductivity above 2 eV is also noticeably reduced at $T < T^{\mathrm{Curie}} \approx 180$ K, and the missing spectral weight is redistributed to energies below 2 eV. However, all the spectral weight is accumulated in a finite-energy peak with a maximum around 0.65 eV and a second weaker maximum around 1.35 eV at 10 K. Both peaks are also present in the paramagnetic state at 200 and 300 K, albeit at a higher energy (by ~0.35 eV) and with a significantly reduced spectral weight. A corresponding behavior was previously observed for a $\mathrm{La}_{0.9}\mathrm{Sr}_{0.1}\mathrm{MnO}_3$ single crystal from the insulating ferromagnetic part of the phase diagram [67]. The pronounced low energy band has been interpreted in terms of ferromagnetic polarons that are pinned to regions with a specific kind of local orbital order that favors the double-exchange interaction [24,66]. Notably, the low energy tail of this relatively narrow band does not reach the origin and therefore does not contribute to the dc conductivity in the ferromagnetic state. This agrees with the insulatorlike T dependence of the dc resistance, as shown in Fig. 7(e). The spectral weight of this polaronic band amounts to about $3 \times 10^6\ \Omega^{-1}\ \mathrm{cm}^{-2}$, yielding $N_{\mathrm{eff}} \approx 1.23 \times 10^{21}\ \mathrm{cm}^{-3}$ or 0.08 electrons per Mn ion. The ratio of the redistributed spectral weight of $3.0/4.6 \approx 0.65$ for the 0.30 mbar grown samples in the as-grown and the oxygen-annealed states roughly follows one of the low-temperature ferromagnetic moment in Fig. 10 of $(3.7/4.1)^2 \approx 0.81$. This is consistent with the point of view that in both samples, despite their different electronic properties, the double-exchange mechanism is at the heart of the ferromagnetic order.

Figure 11(c) shows that a qualitatively similar behavior is observed for the 0.11 mbar as-grown LMO film, which is also in a ferromagnetic insulating state according to the resistance and magnetization data in Figs. 7(a) and 8(a). The lowest interband transition again exhibits a sizeable softening from 1.65 eV at 200 K to 1.4 eV at 10 K that is accompanied by a

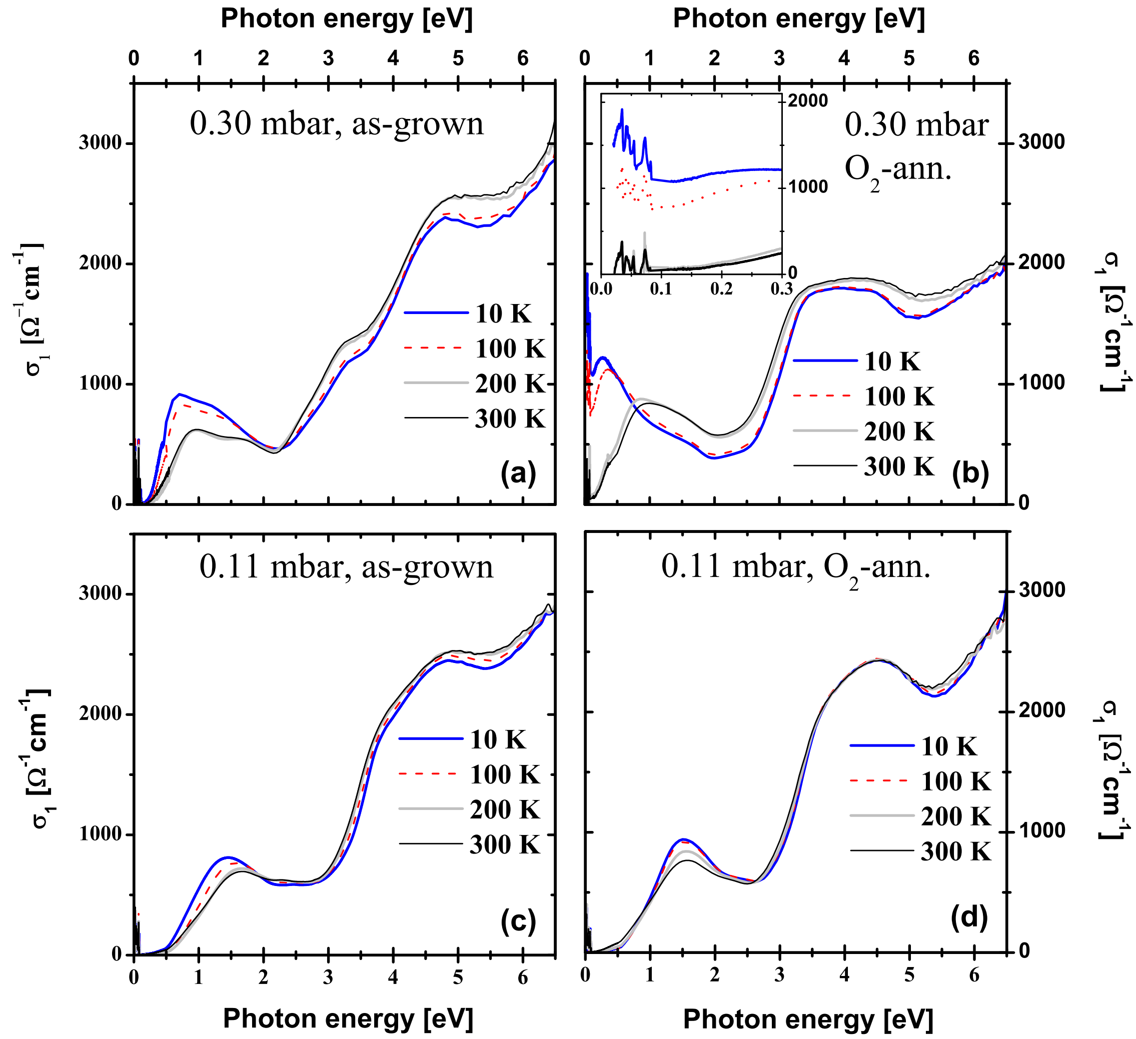

FIG. 11. (Color online) Temperature dependence of the real part of the optical conductivity, σ_1, for (a), (b) the most La-deficient and (c), (d) the most Mn-deficient LMO films. Insert: magnification of the low-energy region showing the free carrier response for the most La-deficient oxygen-annealed sample.

large spectral weight increase of about $1.7 \times 10^6\ \Omega^{-1}\ \mathrm{cm}^{-2}$, corresponding to $N_{\mathrm{eff}} \approx 0.69 \times 10^{21}\ \mathrm{cm}^{-3}$ or 0.045 electrons per Mn ion. This spectral weight is also accumulated from a broad range of frequencies between 2 and 6.5 eV. This is clearly seen in the conductivity difference spectra shown in Fig. 12(b). The ratio of the redistributed spectral weight to that of the 0.30 mbar O_2-annealed sample of $1.7/4.6 \approx 0.37$ also compares reasonably well with the ratio of the low-temperature ferromagnetic moments in Fig. 10 of $(2.9/4.1)^2 \approx 0.50$.

Figure 11(d) shows the T-dependent spectral weight redistribution of the oxygen-annealed LMO film grown at 0.11 mbar for which the ferromagnetic order is strongly suppressed, as shown in Figs. 8(b) and 9(a). Notably, even in this weakly ferromagnetic sample, the optical spectra reveal a redistribution of spectral weight from high energies above 2 eV toward the lowest interband transition around 1.55 eV. The redistributed spectral weight amounts to $\sim 1 \times 10^6\ \Omega^{-1}\ \mathrm{cm}^{-2}$ yielding $N_{\mathrm{eff}} \approx 0.4 \times 10^{21}\ \mathrm{cm}^{-3}$ or $\sim$0.025 electrons per Mn ion. The main difference with respect to the other three LMO films with sizeable ferromagnetic moments concerns the absence of a softening of this low-energy interband transition in the magnetic state. The mode gains spectral weight and eventually becomes a bit narrower with decreasing temperature, but its center frequency remains almost unchanged.

We note that a similar behavior was previously observed in a detwinned LMO single crystal [71] that was stoichiometric and thus close to the undoped state with a dominant A-type antiferromagnetic order. For light polarization along the ab direction in which the spins are ferromagnetically coupled, it was found that the spectral weight of the lowest interband transition (now located around 2 eV) exhibits a sizeable spectral weight increase below $T^{\text{Néel}} \approx 140$ K. This spectral weight was shown to originate from a second band around 4 eV. The opposite trend with a spectral weight shift toward the high energy bands was observed for light polarization along the c direction in which the spins couple in an antiferromagnetic fashion. This characteristic behavior has been interpreted in terms of a super-exchange model in which these bands have been assigned to intersite d-d transitions [71]. The lowest band around 2 eV corresponds to the high spin transition between the e_g orbitals that is enhanced by ferromagnetic spin correlations between the neighboring Mn sites. Three more bands in the

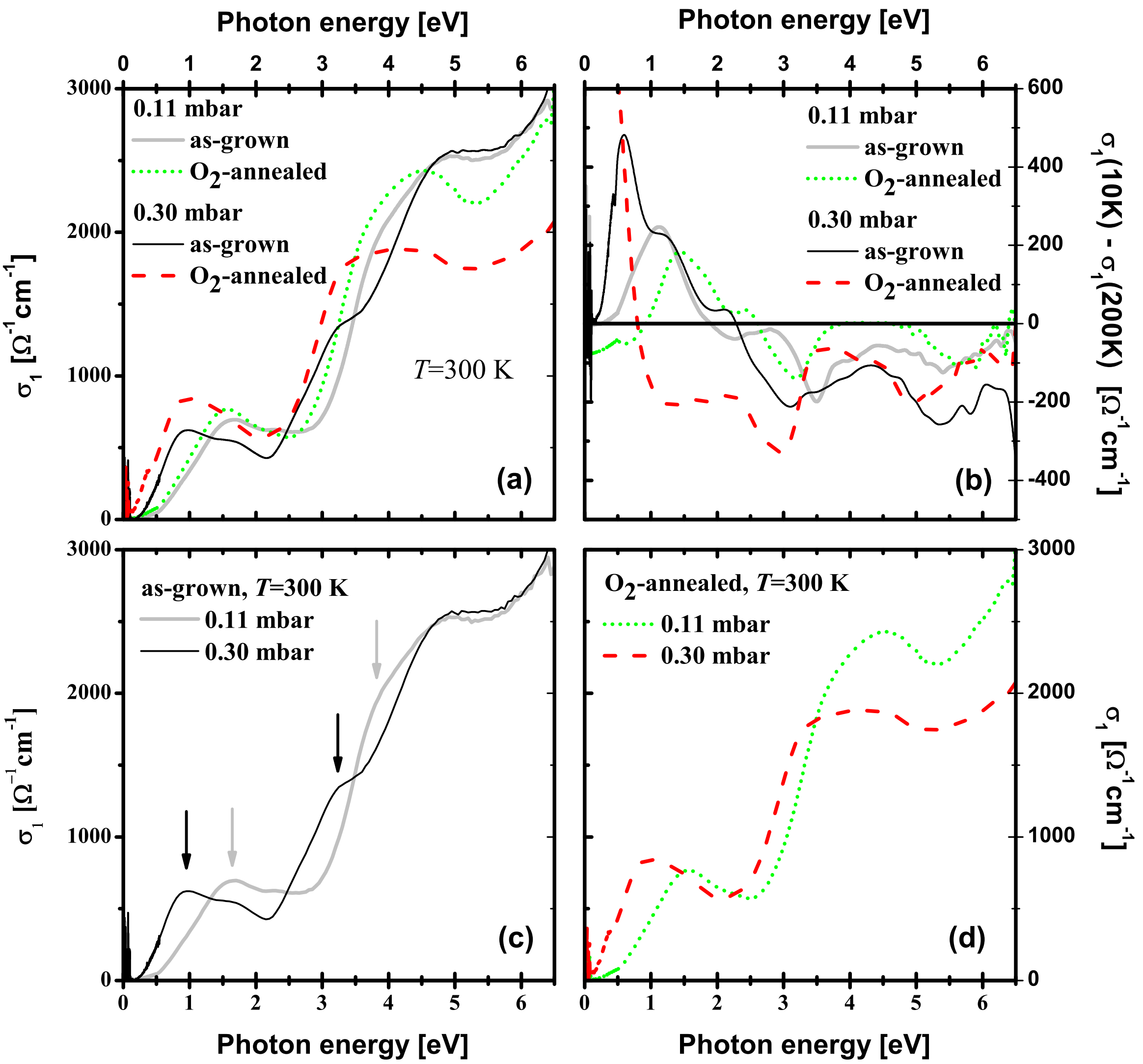

FIG. 12. (Color online) (a) Comparison of the room temperature optical conductivity spectra of the strongly Mn- and La-deficient LMO films before and after the oxygen annealing treatment. (b) Difference spectra of the conductivity in the magnetic state at $T = 10$ K and the paramagnetic state at $T = 200$ K. Positive (negative) values correspond to a spectral weight gain (decrease). (c) Comparison of the room temperature spectra of the as-grown Mn- and La-deficient samples grown at 0.11 and 0.30 mbar of oxygen pressure, respectively. Arrows mark the position of the high-spin and low-spin intersite *d*-*d* transitions that are strongly affected by the cation vacancies. (d) Corresponding spectra for the oxygen-annealed samples.

range of 4 to 6 eV (shifted up by Hund's coupling) have been assigned to the corresponding low-spin transitions that are suppressed by the ferromagnetic spin correlations.

The similar trend observed in our O_2-annealed LMO film deposited at 0.11 mbar suggests that it may also be governed by *A*-type antiferromagnetic correlations. We emphasize that this LMO film is strongly hole doped and thus is far from the undoped region where the *A*-type antiferromagnetic order occurs in stoichiometric samples [20]. This hole doping is evident from the TEP, and it is also consistent with the decrease in resistance upon oxygen annealing and the related decrease of the lattice parameter. It is also evident from the optical spectra, as can be seen in Fig. 12(a), which compares the room temperature spectra of all four LMO films. The oxygen annealing gives rise to a pronounced redshift of the low-energy bands in the range of 1 to 1.5 eV and 3 to 3.5 eV that correspond to the low- and high-spin intersite transitions between the e_g levels. Such a redshift of these bands upon increasing hole doping was also observed in $La_{1-x}(Ca,Sr)_xMnO_3$ single crystals where it was explained in terms of an overall decrease of the Madelung potential upon hole doping [67,68,70]. Even a similar decrease of the conductivity above 5 eV has been observed upon hole doping, which is thought to arise from a further broadening of a very broad peak with a maximum above 6.5 eV that is related to an on-site *p*-*d* transition between the oxygen and Mn bands.

The optical spectra also reveal important differences in these intersite *d*-*d* transitions between the most Mn- and the La-deficient films grown at 0.11 and 0.30 mbar of oxygen partial pressure, respectively. Figure 12(c) shows that for the as-grown samples, the high-spin intersite transition between the e_g levels is shifted from about 1.65 eV in the Mn-deficient samples (0.11 mbar) to about 0.95 eV in the La-deficient samples (0.30 mbar). In the latter, a remnant of the 1.65 eV peak is still visible, which suggests that in addition to the high concentration of La vacancies it contains a small amount of Mn vacancies. A similarly large shift is observed for the bands at 3.85 eV in the Mn-deficient samples and at 3.2 eV in the La-deficient samples that arise from the corresponding low-spin transitions. These sizeable energy differences are most likely caused by the very different effects that the Mn and La vacancies have on the spatially extended nature of the initial and final e_g states. The considerable hardening for the case of the Mn vacancies confirms that they have a much stronger localization effect on the doped holes than the La vacancies.

IV. CONCLUSIONS

In this paper, we have illustrated that the cationic stoichiometry of $LaMnO_{3+\delta}$ films grown by PLD depends in a systematic way on the deposition conditions, namely on the oxygen partial pressure. Samples grown at $p(O_2) \leqslant 0.25$ mbar reveal a Mn deficiency that increases with decreasing $p(O_2)$. The samples grown at $p(O_2)$ of 0.30 mbar are strongly La deficient. The oxygen content in the films can be modified by the postdeposition annealing in flowing oxygen. The combination of these approaches allows one to prepare LMO samples with controlled chemical compositions that in turn determine the electrical and magnetic properties. It has been shown that depending on the cationic stoichiometry and oxygen content, the studied LMO films exhibit similar trends in the properties reported for LMO powders: The Mn-deficient samples exhibit insulating thermal behavior of resistivity and weaker ferromagnetism than La-deficient samples, which have lower resistivity values and become metallic at low temperatures when sufficiently oxygenated. The obtained results represent an easy and versatile approach to tailor the properties of PLD-grown LMO thin films according to the requirements for specific applications.

ACKNOWLEDGMENTS

We acknowledge Yves-Laurent Mathis for technical support during the measurements at the infrared beamline of the ANKA synchrotron at KIT in Germany. This work has been supported by the Schweizer Nationalfonds (SNF) Grant No. 200020-140225 and the National Centre of Competence in Research "Materials with Novel Electronic Properties–MaNEP". One of the authors (PTD) would like to thank the Indo-Swiss Joint Research Program (ISJRP, Research Fellowship Grant No. RF30) and the Council of Scientific and Industrial Research (CSIR) for financial support.

APPENDIX

In the hole doped $La_{1-x}(Sr,Ca)_xMnO_3$ system, the phase diagram of the electronic and magnetic properties is well established and evolves as follows. With increasing hole doping, p, the ferromagnetic moment increases steadily from about 0.2 μ_B per Mn ion at $p = 0$, where it arises from a weak canting of the A-type antiferromagnetic order to about 2–2.5 μ_B per Mn ion around $p \approx 0.1$–0.15 [4,72,73]. In this doping range the samples still exhibit a very high resistivity with an insulatorlike temperature dependence that is commonly interpreted in terms of an activated polaronic transport mechanism [4]. This insulating ferromagnetic state is thought to arise from clusters around the Mn^{+4} ions in which the Jahn-Teller distortion is replaced by a special kind of orbital order which enables a short-ranged double-exchange interaction [24,66]. Upon further hole doping to $0.2 \leqslant p \leqslant 0.4$, as these ferromagnetic clusters develop a sizeable overlap, an itinerant long-range ferromagnetic order emerges in which the orbital order and the Jahn-Teller distortion are suppressed. The ferromagnetic moment reaches values close to the theoretical limit of $(4\text{-}p)\mu_B$ per Mn ion, and the Curie temperature increases to values as high as $T^{\text{Curie}} \approx 270$ and 370 K in $La_{0.67}Ca_{0.33}MnO_3$ and $La_{0.67}Sr_{0.33}MnO_3$, respectively [64]. This regime of the phase diagram is also well known for the CMR effect, which is a result of the competition between the long-range double-exchange interaction, favoring the itinerant ferromagnetic state, and the local Jahn-Teller distortions, tending to localize the charge carries thus giving rise to an upturn of the resistivity with decreasing temperature in the paramagnetic regime at $T > T^{\text{Curie}}$.

Similar phase diagrams have been reported for LMO samples with cation vacancies [20,24,27,29,32]. In truly stoichiometric LMO, all Mn ions have a single oxidation state of +3. The material is a Mott insulator, and it exhibits a large Jahn-Teller distortion of the MnO_6 octahedra and a subsequent orbital order that leads to A-type antiferromagnetism with a Néel temperature of about 140 K [20,74]. In bulk LMO materials the cationic ratio of La/Mn ions is usually close to unity as it is predetermined by the stoichiometric mixture of the starting materials from which the samples are synthesized [20,21,26]. A significant concentration of La and Mn vacancies (in equal amounts) is still frequently found, especially in samples that are prepared in an oxidizing atmosphere [20,21]. Often these are expressed in terms of an excess oxygen content, δ, which represents the equal amounts of Mn and La vacancies and accounts for the resulting concentration of Mn^{4+} ions [20,24,27,29,32]:

$$\begin{aligned} LaMnO_{3+\delta} &= LaMn^{3+}_{(1-2\delta)}Mn^{4+}_{2\delta}O_{3+\delta} \\ &= \frac{3+\delta}{3}La_{3/(3+\delta)}Mn^{3+}_{(3-6\delta)/(3+\delta)}Mn^{4+}_{6\delta/(3+\delta)}O_3. \end{aligned} \tag{A1}$$

In discussing our results, we do not use this notation in terms of the excess oxygen content, δ, but, for the sake of clarity, we rather speak of La and Mn vacancies. Often we will also refer to the concentration of Mn^{4+} ions or the corresponding hole doping level, p. Depending on the preparation and annealing conditions, some LMO samples may also contain oxygen vacancies, which counteract the hole doping effect of the cationic vacancies (they will mostly reside in unit cells with a missing La or Mn ion). In LMO the hole doping is caused by the cationic vacancies, according to Eq. (A1). The missing La^{3+} or Mn^{3+} ions both give rise to similar hole doping effects. The Mn^{3+} vacancies also act as strong localization centers for the holes and severely reduce the strength of the ferromagnetic exchange interaction, especially at high doping levels [20,21]. For the La^{3+} vacancies the corresponding impurity effect is significantly weaker. This difference can be understood in terms of the disruption of the network of Mn-O-Mn bonds, which is essential for the charge transport and also for the ferromagnetic interaction based on the double-exchange mechanism.

In the insulating part of the doping phase diagram, the disorder effect due to the Mn vacancies seems to be less important since they do not lead to fundamental changes of the electronic and magnetic properties. A sizeable ferromagnetic order develops here even in samples in which the hole doping is mainly caused by the Mn vacancies [21]. Albeit, the magnitude of the ferromagnetic moment is somewhat smaller than in samples that are predominantly doped with La vacancies [21]. On the contrary, at higher doping levels of $p > 0.2$, the disorder effect of the Mn vacancies plays a very prominent role and gives rise to a fundamental change of the electronic and magnetic properties. In samples with a large amount of Mn vacancies the itinerant ferromagnetic phase is absent and replaced with a glassy magnetic state, which exhibits signatures of disorder and frustration [24]. The charge carriers in these samples remain localized [20,21]. This is very different from the samples in which the same hole doping ($p > 0.2$) is caused by a corresponding amount of La vacancies. Here an itinerant ferromagnetic state can develop similar to the case of $La_{1-x}(Ca,Sr)_xMnO_3$ [21].

---

[1] R. von Helmolt, J. Wecker, B. Holzapfel, L. Schultz, and K. Samwer, Phys. Rev. Lett. **71**, 2331 (1993).
[2] S. Jin, T. H. Tiefel, M. McCormack, R. A. Fastnacht, R. Ramesh, and L. H. Chen, Science **264**, 413 (1994).
[3] A. P. Ramirez, J. Phys.: Condens. Matter **9**, 8171 (1997).
[4] J. M. D. Coey, M. Viret, and S. von Molnar, Adv. Phys. **48**, 167 (1999).
[5] A. J. Millis, Nature **392**, 147 (1998).
[6] Y. Tokura and Y. Tomioka, J. Magn. Magn. Mater. **200**, 1 (1999).
[7] J. H. Park, E. Vescovo, H. J. Kim, C. Kwon, R. Ramesh, and T. Venkatesan, Nature **392**, 794 (1998).
[8] S. W. Cheong and M. Mostovoy, Nat. Mater. **6**, 13 (2007).
[9] T. Venkatesan, M. Rajeswari, Z. W. Dong, S. B. Ogale, and R. Ramesh, Philos. Trans. R. Soc. London A **356**, 1661 (1998).
[10] Y. Fujisaki, Jpn. J. Appl. Phys. **52**, 040001 (2013).
[11] A. Asamitsu, Y. Tomioka, H. Kuwahara, and Y. Tokura, Nature **388**, 50 (1997).
[12] W. R. Zhang, A. P. Chen, F. Khatkhatay, C. F. Tsai, Q. Su, L. Jiao, X. H. Zhang, and H. Y. Wang, ACS Appl. Mater. Interfaces **5**, 3995 (2013).
[13] M. P. de Jong, V. A. Dediu, C. Taliani, and W. R. Salaneck, J. Appl. Phys. **94**, 7292 (2003).
[14] R. J. H. Voorhoeve, J. P. Remeika, and D. W. Johnson, Science **180**, 62 (1973).
[15] R. J. H. Voorhoeve, J. P. Remeika, B. T. Matthias, and P. E. Freeland, Science **177**, 353 (1972).
[16] E. G. Vrieland, J. Catal. **32**, 415 (1974).
[17] J. H. Chen, M. Q. Shen, X. Q. Wang, G. S. Qi, J. Wang, and W. Li, Appl. Catal. B **134**, 251 (2013).
[18] J. Hoppler, J. Stahn, C. Niedermayer, V. K. Malik, H. Bouyanfif, A. J. Drew, M. Rossle, A. Buzdin, G. Cristiani, H. U. Habermeier *et al.*, Nat. Mater. **8**, 315 (2009).
[19] J. Chakhalian, J. W. Freeland, G. Srajer, J. Strempfer, G. Khaliullin, J. C. Cezar, T. Charlton, R. Dalgliesh, C. Bernhard, G. Cristiani *et al.*, Nature Physics **2**, 244 (2006).
[20] J. Topfer and J. B. Goodenough, J. Solid State Chem. **130**, 117 (1997).
[21] J. Topfer and J. B. Goodenough, Chem. Mater. **9**, 1467 (1997).
[22] P. A. Joy, C. R. Sankar, and S. K. Date, J. Phys.: Condens. Matter **14**, 4985 (2002).
[23] P. A. Joy, C. R. Sankar, and S. K. Date, J. Phys.: Condens. Matter **14**, L663 (2002).
[24] C. Ritter, M. R. Ibarra, J. M. DeTeresa, P. A. Algarabel, C. Marquina, J. Blasco, J. Garcia, S. Oseroff, and S. W. Cheong, Phys. Rev. B **56**, 8902 (1997).
[25] B. C. Tofield and W. R. Scott, J. Solid State Chem. **10**, 183 (1974).
[26] J. A. M. van Roosmalen, P. Vanvlaanderen, E. H. P. Cordfunke, W. L. Ijdo, and D. J. W. Ijdo, J. Solid State Chem. **114**, 516 (1995).
[27] J. A. M. van Roosmalen, E. H. P. Cordfunke, R. B. Helmholdt, and H. W. Zandbergen, J. Solid State Chem. **110**, 100 (1994).
[28] J. A. M. van Roosmalen and E. H. P. Cordfunke, J. Solid State Chem. **110**, 106 (1994).
[29] J. A. M. van Roosmalen and E. H. P. Cordfunke, J. Solid State Chem. **110**, 109 (1994).
[30] J. A. M. van Roosmalen and E. H. P. Cordfunke, J. Solid State Chem. **110**, 113 (1994).
[31] J. A. M. van Roosmalen and E. H. P. Cordfunke, J. Solid State Chem. **93**, 212 (1991).
[32] J. H. Kuo, H. U. Anderson, and D. M. Sparlin, J. Solid State Chem. **83**, 52 (1989).
[33] J. H. Kuo, H. U. Anderson, and D. M. Sparlin, J. Solid State Chem. **87**, 55 (1990).
[34] A. Gupta, T. R. McGuire, P. R. Duncombe, M. Rupp, J. Z. Sun, W. J. Gallagher, and G. Xiao, Appl. Phys. Lett. **67**, 3494 (1995).
[35] P. Murugavel, J. H. Lee, J. G. Yoon, T. W. Noh, J. S. Chung, M. Heu, and S. Yoon, Appl. Phys. Lett. **82**, 1908 (2003).
[36] H. S. Kim and H. M. Christen, J. Phys.: Condens. Matter **22**, 146007 (2010).
[37] W. S. Choi, Z. Marton, S. Y. Jang, S. J. Moon, B. C. Jeon, J. H. Shin, S. S. A. Seo, T. W. Noh, K. Myung-Whun, H. N. Lee *et al.*, J. Phys. D **42**, 165401 (2009).
[38] W. S. Choi, D. W. Jeong, S. Y. Jang, Z. Marton, S. S. A. Seo, H. N. Lee, and Y. S. Lee, J. Korean Phys. Soc. **58**, 569 (2011).
[39] C. Aruta, M. Angeloni, G. Balestrino, N. G. Boggio, P. G. Medaglia, A. Tebano, B. Davidson, M. Baldini, D. Di Castro, P. Postorino *et al.*, J. Appl. Phys. **100**, 023910 (2006).
[40] P. Orgiani, C. Aruta, R. Ciancio, A. Galdi, and L. Maritato, Appl. Phys. Lett. **95**, 013510 (2009).
[41] A. Kleine, Y. Luo, and K. Samwer, Europhys. Lett. **76**, 135 (2006).
[42] K. Uusi-Esko and M. Karppinen, Chem. Mater. **23**, 1835 (2011).
[43] H. Khanduri, M. C. Dimri, S. Vasala, S. Leinberg, R. Lohmus, T. V. Ashworth, A. Mere, J. Krustok, M. Karppinen, and R. Stern, J. Phys. D **46**, 175003 (2013).

[44] G. Kartopu and M. Es-Souni, J. Appl. Phys. **99**, 033501 (2006).

[45] R. Todorovska, N. Petrova, D. Todorovsky, and S. Groudeva-Zotova, Appl. Surf. Sci. **252**, 3441 (2006).

[46] M. Gibert, P. Zubko, R. Scherwitzl, J. Iniguez, and J. M. Triscone, Nat. Mater. **11**, 195 (2012).

[47] T. Golod, A. Rydh, V. M. Krasnov, I. Marozau, M. A. Uribe-Laverde, D. K. Satapathy, T. Wagner, and C. Bernhard, Phys. Rev. B **87**, 134520 (2013).

[48] D. K. Satapathy, M. A. Uribe-Laverde, I. Marozau, V. K. Malik, S. Das, T. Wagner, C. Marcelot, J. Stahn, S. Bruck, A. Ruhm *et al.*, Phys. Rev. Lett. **108**, 197201 (2012).

[49] J. H. Haeni, P. Irvin, W. Chang, R. Uecker, P. Reiche, Y. L. Li, S. Choudhury, W. Tian, M. E. Hawley, B. Craigo *et al.*, Nature **430**, 758 (2004).

[50] D. B. Chrisey and J. R. Huber, *Pulsed Laser Deposition of Thin Films* (John Wiley & Sons, Inc., New York, 1994).

[51] J. Hoppler, J. Stahn, H. Bouyanfif, V. K. Malik, B. D. Patterson, P. R. Willmott, G. Cristiani, H. U. Habermeier, and C. Bernhard, Phys. Rev. B **78**, 134111 (2008).

[52] V. K. Malik, I. Marozau, S. Das, B. Doggett, D. K. Satapathy, M. A. Uribe-Laverde, N. Biskup, M. Varela, C. W. Schneider, C. Marcelot *et al.*, Phys. Rev. B **85**, 054514 (2012).

[53] A. S. Arrot, in *Ultrathin Magnetic Structures I*, edited by J. A. C. Bland and B. Heinrich (Springer-Verlag, Berlin, Heidelberg, 2005), p. 177.

[54] Y. Wang and M. Nastasi, *Handbook of Modern Ion Beam Materials Analysis* (Materials Research Society, Warrendale, 2010).

[55] I. Marozau, A. Shkabko, M. Döbeli, T. Lippert, D. Logvinovich, M. Mallepell, C. Schneider, A. Weidenkaff, and A. Wokaun, Materials **2**, 1388 (2009).

[56] M. Döbeli, J. Phys.: Condens. Matter **20**, 264010 (2008).

[57] L. R. Doolittle, Nucl. Instrum. Methods Phys. Res., Sect. B **15**, 227 (1986).

[58] W. H. Bragg and W. L. Bragg, Proc. R. Soc. London, A **88**, 428 (1913).

[59] C. Bernhard, J. Humlicek, and B. Keimer, Thin Solid Films **455-456**, 143 (2004).

[60] JA Woollam Co. Inc., http://www.jawoollam.com.

[61] P. R. Willmott and J. R. Huber, Rev. Mod. Phys. **72**, 315 (2000).

[62] T. Lippert, in *Photon-based Nanoscience and Nanobiotechnology*, edited by J. J. Dubowski and S. Tanev (Springer, Amsterdam, 2006), p. 267.

[63] R. D. Shannon, Acta Crystallogr., Sect. A: Found. Crystallogr. **32**, 751 (1976).

[64] G. J. Snyder, R. Hiskes, S. DiCarolis, M. R. Beasley, and T. H. Geballe, Phys. Rev. B **53**, 14434 (1996).

[65] H. J. Goldsmid, *Introduction to Thermoelectricity* (Springer-Verlag, Berlin, Heidelberg, 2010).

[66] R. Kilian and G. Khaliullin, Phys. Rev. B **60**, 13458 (1999).

[67] Y. Okimoto, T. Katsufuji, T. Ishikawa, T. Arima, and Y. Tokura, Phys. Rev. B **55**, 4206 (1997).

[68] M. Quijada, J. Černe, J. R. Simpson, H. D. Drew, K. H. Ahn, A. J. Millis, R. Shreekala, R. Ramesh, M. Rajeswari, and T. Venkatesan, Phys. Rev. B **58**, 16093 (1998).

[69] N. Furukawa, J. Phys. Soc. Jpn. **64**, 3164 (1995).

[70] K. Takenaka, K. Iida, Y. Sawaki, S. Sugai, Y. Moritomo, and A. Nakamura, J. Phys. Soc. Jpn. **68**, 1828 (1999).

[71] N. N. Kovaleva, A. V. Boris, C. Bernhard, A. Kulakov, A. Pimenov, A. M. Balbashov, G. Khaliullin, and B. Keimer, Phys. Rev. Lett. **93**, 147204 (2004).

[72] A. Urushibara, Y. Moritomo, T. Arima, A. Asamitsu, G. Kido, and Y. Tokura, Phys. Rev. B **51**, 14103 (1995).

[73] H. Kawano, R. Kajimoto, M. Kubota, and H. Yoshizawa, Phys. Rev. B **53**, 2202 (1996).

[74] Y. Tokura and N. Nagaosa, Science **288**, 462 (2000).